Journal of
Electrical & Electronic Systems

Ali et al., J Electr Electron Syst 2017, 6:4
DOI: 10.4172/2332-0796.1000242

Research Article Open Access

0 μ Magnetic Polarizer for 1.5-T MRI

Hassan Ali*, Erik Forsberg and Hu Jun

Department of Optical Engineering, State Key Lab of Modern Optical Instrumentation, Centre for Optical and Electromagnetic Research, Zhejiang University, Hangzhou 310058, China

Abstract

Study of human pathologies and acquisition of anatomical images without any surgical intervention inside human body is possible because of magnetic resonance imaging (MRI). This work exploits the notable properties of zero permeability (0 μ) split ring resonators (SRR) metamaterial (MM) magnetic polarizer which could distort, control and reject uniform RF (radio frequency) magnetic field for 1.5-T MRI systems. Unique polarizer was proposed to etch on PCB (printed circuit board) slabs for compact thickness of 5 mm only. In addition, polarizer was loaded with novel combination of parametric elements (capacitors, inductors) which could made the structure tunable to achieve resonance at different working frequencies. We achieved the value of relative permeability, μ_r=0.02+j0.1 for 1.5-T MRI systems at 63.85 MHz. Furthermore polarizer, when used with MRI scanner at optimized position, uniformly redistributed and enhanced the magnetic field while lowered specific absorption ratio (SAR), induced electric field, power dissipation, and locally improved SNR (signal to noise ratio) at the scanned region of phantom {real case was human body}. The polarizer minimized the damaging effects of RF energy absorption in human tissue and prevented them from heating.

Keywords: MRI; Zero permeability; SRR; SAR

Introduction

One of substantial challenge for imaging of objects and bodies with non-invasive techniques is well tackled by MRI systems, which plays an important role to characterize symptoms and diagnosis of the nature of illness in human body [1,2]. These systems offer different signal strengths of transient transverse magnetic field (B_1) and static magnetic field (B_0) for different imaging requirements to identify the biological structures. Scientists adopted different techniques to surpass MRI system efficiency by maintaining B_1 without increasing B_0 to avoid the risk of tissue heating and specific absorption ratio (SAR) due to absorbed power in human tissue at greater B_0 [3-15]. They concluded that greater B_0 of MRI system was harmful for human body which caused nausea and giddiness [16]. The homogeneity of magnetic field (B-field) and SNR at region of interest, ROI depended upon B_1 which was mainly governed by transmit/receive MR coils of MRI system. B_1 perturb ROI's protons from equilibrium which yielded in image acquisition at receiver MR coil [17-19].

Metamaterials tremendously exploits electromagnetic properties which were absent in natural materials [20-22]. Theoretically and experimentally proved that metamaterials when used with MRI systems has improved image resolution, image acquisition time and image quality inside the human body [23-31]. We still believe that metamaterials for MRI systems contain much hidden potential which should be expose in future research.

In the present work, we explored the significance of 0 μ SRRs magnetic polarizer, when used with MRI system; distort, reject and redistributed the RF field efficiently towards ROI and could locally enhanced B_1 field at ROI without increasing B_0. This property was absent in previous work of negative permeability -μ metamaterial lenses [26]. Polarizer with compact thickness of only 5 mm and novel combination of parametric elements (capacitors, inductors), exhibited resonance at very low working frequency of 63.85 MHz, which was the frequency of operation for 1.5-T MRI systems. Use of parametric elements in design yielded in reduction of propagation losses which improved SNR at ROI and finally improved B field in that region. We presented analysis for 0 μ polarizer when used with MRI test bed setup that showed superior B field and SNR at ROI inside phantom in comparison to the equivalent setup, where the polarizer was absent. In addition, we proposed optimized placement of the MR coil and polarizer in accordance with ROI, which could reduce the SAR and enhanced B field at ROI.

The paper was organized as follows; section 2; Geometrical study of B_0 at MR coil and B_1 at ROI due to 0 μ magnetic polarizer; section 3; Relative permeability $\{\mu_r\}$ parameters retrieval method and plot analysis; section 4; Design configuration and circuit model calculations; section 5; B-Field and SNR comparison; Experimental Test bed Setup Analysis; The paper was concluded in section 6.

Geometrical Study of B_0 at MR Coil and B_1 at ROI due to 0 μ Magnetic Polarizer

Figure 1a depicted magnetic resonance (MR) coil facing Z-plane and carrying current I due to E (applied electric field). The electromotive force (emf) produced by MR coil as Lorentz magnetic force generated static magnetic field B_0 around MR loop coil [31,32]. Magnetic dipole D as magnetically susceptible material was placed at the distance x from MR coil. Geometry of MR coil as torus had diameter $d_M\{d_M=2(r_M\ r'_M)\}$ with outer radius r_M and inner radius r'_M respectively. Thickness of MR coil was taken as $t_M=2\ r'_M$. By the help of Biot-Savart's Law [32], we studied static magnetic field B_0.

$$B_0 = \frac{2\mu_0 IA}{4\pi U^3} \quad (1)$$

Where area $A=\pi r^2$ of the circular MR coil. We further attributed $IA=D_m$. Now we consider 0 μ magnetic polarizer as shown in Figure 1b, where inductive power transfer was strictly contingent upon strong

***Corresponding author:** Dr. Hassan Ali, Department of Optical Engineering, State Key Lab of Modern Optical Instrumentation, Centre for Optical and Electromagnetic Research, Zhejiang University, Hangzhou 310058, China, Tel: +86-13251023857; E-mail: drali@zju.edu.cn

Received November 12, 2017; **Accepted** December 05, 2017; **Published** December 12, 2017

Citation: Ali H, Forsberg E, Jun H (2017) 0 μ Magnetic Polarizer for 1.5-T MRI. J Electr Electron Syst 6: 242. doi: 10.4172/2332-0796.1000242

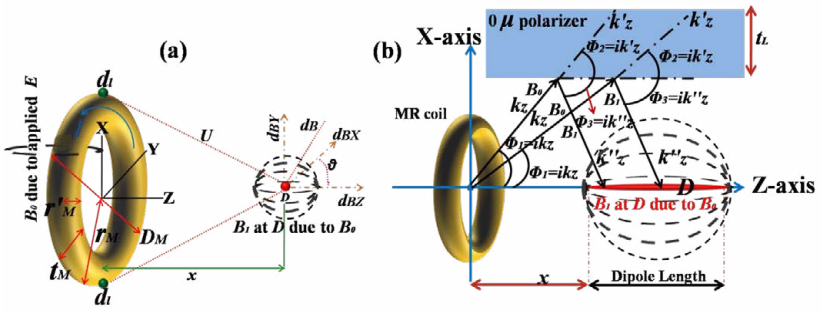

Figure 1: (a) Transient transverse magnetic field B_1 at D due to static magnetic field B_0. Generated B_1 at D due to B_0 because of applied electric field E at MR coil of MRI system, (b) 0 μ magnetic polarizer transmitted TM component of evanescent wave k_z with angle ϕ_1 to $k_z^{'}$ with angle ϕ_2. Furthermore, 0 μ magnetic polarizer rejected TE component of evanescent wave k_z with angle ϕ_1 to $k_z^{''}$ with angle ϕ_3, finally yielded in restoration of B_0 to B_1 at D.

coupling of evanescent waves between polarizer's medium due to applied static magnetic field B_0 created by transmitting loop MR coil (Figure 1).

In consequence of B_0, current I was induced in each SRR of polarizer to resonate a structure at 63.85 MHz with 0 μ values and restored B_0 to transient transverse magnetic field B_1 at D. We know that wave vectors of EM wave had real $\left\{R_e\left[n(\omega)\right]\right\}$ and imaginary $\left\{I_{mg}\left[n(\omega)\right]\right\}$ parts for a certain angular frequency $(\omega = 2\pi f)$. We calculated the refractive index $\left[n(\omega)\right]$ from $\left\{R_e\left[n(\omega)\right]\right\}$ and $\left\{I_{mg}\left[n(\omega)\right]\right\}$ to calculate the relative permittivity $\left[\varepsilon_r(\omega)\right]$ and relative permeability $\left[\mu_r(\omega)\right]$ for our designed medium. It was obvious that large $\left\{I_{mg}\left[n(\omega)\right]\right\}$ of the EM wave yielded in high damping factor γ and more losses in wave propagation [27-30]. To satisfy the conditions for 0 μ magnetic polarizer, $\left\{I_{mg}\left[n(\omega)\right]\right\}$ must be small enough so that EM wave propagation might exist within the medium with very low damping factor γ. In result, $R_e\left[\mu_r(\omega)\right]$ of the evanescent EM wave had a large slope value and could be zero with very small refractive index $\left[n(\omega)\right]$ and very small $\left\{I_{mg}\left[n(\omega)\right]\right\}$ respectively [33]. Figure 1b gave geometrical study of 0 μ magnetic polarizer whose thickness was t_L and the design facing X-axis transmitted TM component of evanescent wave k_z with angle ϕ_1 to $k_z^{'}$ with angle ϕ_2. Furthermore, 0 μ magnetic polarizer rejected and controlled TE component of evanescent wave with its magnitudes of wave vectors k_z with their angles ϕ_1 to magnitudes of vectors $k_z^{''}$ with their angles ϕ_3, finally yielded in restoration of B_0 to B_1 at D. The incidence of TE plane wave evanescent in X-axis as magnitudes of vectors $k_z^{''}$ with their angles ϕ_3 in the sense of transient transverse magnetic field B_1 was calculated [34].

$$B_1 = \frac{E_{ind}}{\omega\mu_r}\left(k_x z_0 + k_z x_0\right)e^{j\left(k_z z + k_x x\right)} \tag{2}$$

$$E_{ind} = E_0^{inc} e^{j\left(k_z z + k_x x\right)} \tag{3}$$

Eind was induced electric field at D, $k_x z_0$ and $k_x z_0$ were normal components of wave vectors k_x along Z-axis and k_z along X-axis, respectively. $k_z z + k_z x = k_z^{*}$ was magnitudes of wave vectors with their phase angles ϕ_3 at D from the direction of polarizer. $k_x = \sqrt{k_0^2 - k_z^2}$, $k_x = \sqrt{k_0^2 - k_x^2}$, where $Imag\left\{k_z^{*}\right\} \cong 0$. This yielded in $R_e\left[\mu_r(\omega)\right] \cong I_{mg}\left[\mu_r(\omega)\right] \cong 0$, where μ_r was the relative permeability of our design and ω was angular frequency of incident evanescent wave. E_0^{inc} was an incident electric field applied to MR coil. Then we calculated transfer function incidence of TE plane wave vectors $k_z^{''}$ [33].

$$T = \frac{\dfrac{4k_z^{''}k_z}{\mu_r}e^{-ik_z^{'}t_L}}{\left(k_z^{''} + \dfrac{k_z}{\mu_r}\right)^2 e^{-ik_z t_L} - \left(k_z^{''} - \dfrac{k_z}{\mu_r}\right)^2 e^{ik_z t_L}} \tag{4}$$

Where, $k_z^{''} = 2\pi\dfrac{\mathrm{Cos}\varnothing 3}{\lambda}$ and $k_z = 2\pi n\dfrac{\mathrm{Cos}\varnothing 1}{\lambda}$. λ Was wavelength of the incident wave and $\varnothing 3 = \varnothing 1$. The expression for μ_r was calculated.

$$\mu_r(\omega) = 1 - \frac{\omega_m - \omega_0^2}{\omega^2 - \omega_0^2 + \mathrm{i}\gamma\omega} \tag{5}$$

ω_0 and ω_m were resonant angular frequency (restoring force) and magnetic plasma frequency (switching force) respectively. γ was damping factor. It has been noticed that $\left\{\mathrm{I}_{\mathrm{mg}}\left[n(\omega)\right]\right\}$ played an important role for the designing of 0 $\mu_r(\omega)$ medium and it could be satisfied when $\omega = \omega_m$ with constant damping factor γ [34].

Relative Permeability $\{\mu_r\}$ Parameters Retrieval Method and Plot Analysis

Magnetic dipoles of magnetically susceptible materials aligned themselves in the direction of externally applied B-field which depended upon strength of B-field. In result, those materials were resonant at particular frequencies. For 0 μ magnetic polarizer, we retrieved relevant values from S-parameter measurements through transmission and reflection coefficients [35]. By using boundary conditions as unit cell in CST Microwave studio for our design in frequency domain solver, we analyzed wave vectors k_z, $k_z^{''}$ with their phase angles φ_1, φ_3 of incident wave and finally measured relative permittivity $\varepsilon_r(\omega)$ relative permeability $\mu_r(\omega)$ and refractive index $n(\omega)$ (Figure 2).

$$n = real\ of\left(n\right) + i\left(imaginary\left(n\right)\right) \tag{6}$$

$$\varepsilon = n/\eta \tag{7}$$

$$\mu = n\eta \tag{8}$$

$$\eta = \sqrt{\frac{\left(1+S_{11}\right)^2 - S_{21}^2}{\left(1-S_{11}\right)^2 - S_{21}^2}} \tag{9}$$

$$\text{real of } n = \text{imaginary}\frac{\left[\log\dfrac{S_{21}}{1 - S_{11}\left(\dfrac{\eta-1}{\eta+1}\right)}\right]}{\left(k_z, k_z^{'}\right)t_L} \tag{10}$$

$$\text{imaginary of } n = -\text{real}\left[\frac{\log\dfrac{S_{21}}{1-S_{11}\left(\dfrac{\eta-1}{\eta+1}\right)}}{\left(k_z, k_z^{'}\right)t_L}\right] \tag{11}$$

Where η was the wave impedance of magnetic polarizer. For the targeted frequency of 1.5-T MRI system, we then calculated S_{21} and S_{11} in the frequency range from 30 to 80 MHz for nit cell geometry as described in section 4, for magnetic polarizer. Relative permeability, μ_r=0.02+j0.1 was then calculated and plotted as a function of frequency and depicted in Figure 2a. It was observed and shown in inset of Figure 2b, that real part of magnetic permeability μ_r became nearly zero and resonant in the frequency range from 63.85 MHz to 64.1 MHz.

Design Layout and Circuit Model Computation

A regular array of split ring resonator unit cell arranged in square lattice exhibited strong coupling among themselves due to strong mutual induction and finally reduced propagation losses [36,37]. SRR unit cell was schematically depicted in Figure 3a where three copper rings P_1, P_2 and P_3 were restacked in a way to make 3D symmetry of cubic structure. Figure 3b depicted one side of square SRR copper ring with thickness and width of t_c=0.070 mm and W=0.3 mm respectively. SRR ring was etched on nonmagnetic PCB and loaded with lumped elements e.g., capacitor element c_e=0.13nF and inductor element l_e=37.2nH. The PCB with its material properties had relative permittivity ε_r=2.33, relative permeability μ_r=1, and a thickness t_s=0.381 mm. The side length of the SRR square was S=4.4 mm. Complete design was composed of 3-D array of SRR unit cells having a periodicity a=5 mm, which was then also the lens thickness t_L. It was observed that nonlinear significance of lumped elements enhanced the importance of design to make it resonant at different working frequencies. Lumped elements maintained uniformity of induced currents i_p, in each SRR ring and minimized losses in wave propagation. This mechanism reconstructed the amplitude of incoming signal [29-38]. Specifically inductor supported B field concentration into SRR circuit array by re-linking the field to arrays and finally made uniform formation of induced currents. This uniform formation of induced currents among SRR arrays provided strong mutual induction among them due to strong coupling between arrays [39].

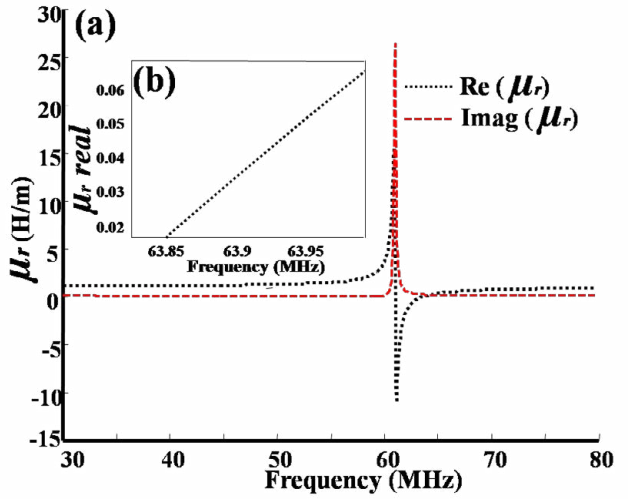

Figure 2: (a) and of 0 μ magnetic polarizer. At resonance the relative permeability was μ_r=0.02+j0.1, (b) At 63.85 MHz, Real part of μ_r exhibited resonance.

Equivalent Circuit model of Figure 3a, was explained in Figure 4, where unit cell composed of three periodically arranged 0 μ polarizer SRR magnetically coupled rings loaded with lumped inductor l_e and lumped capacitor c_e, finally making RLC circuit. The SRR rings of unit cell were named as P_1, P_2 and P_3. The generation of magnetic flux created by the MR coil across SRR rings P_1, P_2 and P_3 depended upon induced currents i_p among P_1, P_2 and P_3 [34]. Figure 4 demonstrated C_p{self capacitance}, L_p{self inductance}, R_p{self resistance} and M_{LP}{mutual inductance between SRR rings P_1, P_2 and P_3} of the unit cell (Figures 3 and 4).

Total flux through each ring was calculated as the sum of external source B flux and flux across SRR rings in the result of induced currents i_p and mutual inductance M_{LP} between SRR rings P_1, P_2 and P_3 of unit cell [40].

$$\Delta_1 = B + \left(\sum_{P_1 \neq P_2} M_{(LP)_{12}} + \sum_{P_1 \neq P_3} M_{(LP)_{13}}\right) i_{P_1} \tag{12}$$

Δ_1=Flux through single SRR, say; P_1, B=Externally produced flux because of MR coil, $M_{(LP)}$=Mutual inductance among P_1P_2 and P_1P_3 in a unit cell respectively, i_{P_1} =Induced current i_p created by external field B at SRR P_1. Flux through single unit cell was derived as:

$$Z_{P'} I_{P'} = \Delta^{'} \tag{13}$$

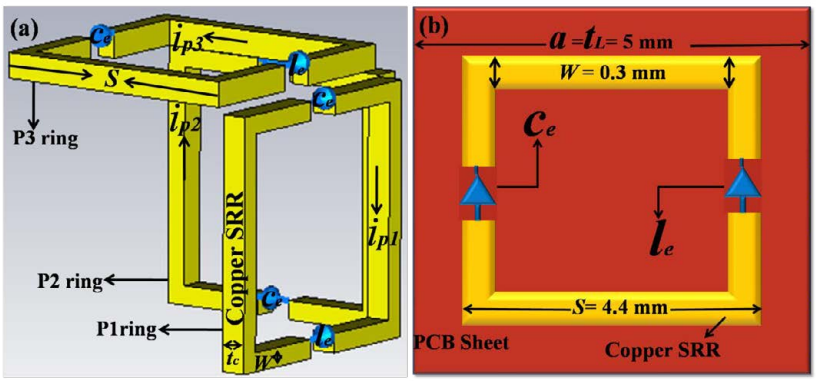

Figure 3: (a) 3-Dimentional view in CST. Unit cell composed of SRRs P_1, P_2, P_3 loaded with lumped elements capacitors c_e & inductors l_e, (b) 2-Dimnentional view of One side of square PCB with periodicity a attached with SRR copper ring, c_e and l_e respectively.

$Z_{P'}$ =impedance of SRR for single unit cell, $I_{P'}$ =Induced currents single unit cell $\left(I_{P'} = i_{P_1} + i_{P_2} + i_{P_3}\right)$, P' =Total SRR rings in unit cell (P_1, P_2, P_3), Δ'=Magnetic flux generated at single unit cell because of external applied field and $\Delta' = \Delta_1 + \Delta_2 + \Delta_3$. We applied the Kirchhoff's voltage law (KVL) on the equivalent circuit model of single unit cell, yielded [40];

$$V_{P'} = i_{P'} R_{P'} + L_{P'} \frac{di_{P'}}{d_t} + \frac{1}{C_{P'}} \int i_{P'} d_t \tag{14}$$

$$Z_{P'} = R_{P'} + \left(j\omega L_{P'} + \frac{1}{j\omega C_{P'}} \right) + j\omega \left(M'_{LP} \right) \tag{15}$$

$V_{P'}$=External voltage applied to polarizer's unit cell, $R_{P'}$=overall self-resistance, $L_{P'}$=overall self-inductance, $C_{P'}$=overall self-capacitance of polarizer's SRR of single unit cell, M'_{LP}=overall mutual inductance among SRR rings, say; P1, P2 and P3. No external voltage was applied to polarizer's structure as input and induced currents i_p were resulted in SRR rings, P', because of externally applied magnetic field created by MR loop coil. In consequence, we took V_P'= 0 volts for polarizer's SRR rings. Self-resistance R, was calculated by considering skin depth δ for polarizer's SRR rings [41].

$$\delta = \sqrt{\frac{1}{\pi f \mu_{r1} \mu_0 \sigma}} \tag{16}$$

δ=Skin depth for copper material, μ_{r1}=1 {relative permeability of copper}, f=resonance frequency for SRR, μ_0=free space relative permeability, σ=copper's conductivity. At 63.85 MHz, $\delta$was calculated as 0.0083 mm for copper SRR ring. The SRR's thickness t_c in our design was 0.070 mm and clearly resulted as $t_c > \delta$. For this purpose, we needed to adopt two certain rules for calculations of self-resistance R_P [42].

$$R_p = \frac{S_1}{\sigma W t_c} \qquad (t_c \le \delta) \tag{17}$$

$$R_p = \frac{S_1}{W} \sqrt{\frac{\pi f \mu_{r1} \mu_0}{\sigma}} \qquad (t_c > \delta) \tag{18}$$

S_1=($\pi \times S \times 1.273$) equivalent length of SRR square ring, W=SRR ring strip width, t_c=Thickness of the SRR copper ring. Then Lp as self-inductance and Cp as self-capacitance of SRR rings in unit cell were calculated [43-46] (Table 1).

$$L_p = \frac{\mu_0 S_1}{4\pi} \left\{ \frac{1}{2 sinh\left(\frac{S_1}{W}\right)} + 2\frac{S_1}{W} \times \frac{1}{2 sinh\left(\frac{W}{S_1}\right)} + \frac{2}{3} \left[\left(\left(\frac{S_1}{W}\right)^2 \right) + \frac{W}{S_1} - \frac{\left(W^2 + S_1^2\right)^{\frac{3}{2}}}{S_1 W^2} \right] \right\} \tag{19}$$

$$C_p = \frac{\varepsilon_0 \varepsilon_r W S_1}{t_s} \tag{20}$$

t_s=PCB thickness, ε_0=Permittivity of free space, ε_r=PCB's Relative permittivity. Finally we calculated M_{LP12} among two SRR rings. We used mutual inductance algorithm in our calculations [46].

$$M_{(LP)12} = \frac{\mu_0}{4\pi} \left\{ \frac{2S}{sinh\left(\frac{S}{S - 2W}\right)} + 2\left[(S - 2W) - \sqrt{(S - 2W)^2 + S^2} \right] \right\} \tag{21}$$

It was deduced from equivalent circuit model in Figure 4 that each polarizer's ring was making RLC series circuit with its elements, (c_e, l_e) and RLC parallel circuit with other rings. Furthermore mutual inductance among SRR rings of unit cell resulted in RLC series circuit. Then total mutual inductance M'_{LP} between the rings was calculated.

$$M'_{LP} = M_{(LP)12} + M_{(LP)23} + M_{(LP)13} \tag{22}$$

Table 1 resulted in stronger overall mutual inductance M'_{LP} among SRR rings, say; (P_1, P_2 and P_3) for single unit cell in comparison with individual self-inductance L_p and overall self-inductance L_P'. These results provided a strong case of coupling of one SRR ring with its neighbors and yielded in surpassed magnetic field in presence of magnetic polarizer. By exploiting eqns. (12-22), we finally calculated overall magnetic flux Δ / unit cell of magnetic polarizer in the consequence of applied magnetic field.

B-Field and SNR comparison; Experimental Test Bed Setup Analysis

Experimental setup for MRI test bed was adopted using commercial COMSOL Multi-physics software as depicted in Figure 5. Magnetic field, B and SNR were measured at magnetically susceptible dipole D, which was positioned at distance x from MR loop coil and located inside phantom. It was studied in the light of Reciprocity theorem that received transient transverse magnetic field B_1 from dipole D was proportional to static magnetic field B_0/unit induced current at that dipole D [47-48]. Noise in the signal was related to SNR and it was observed that due to intrinsically thermally generated noise currents produced noise resistance at dipole D, which resulted in creation of noise in the signal. This noise creation was in direct proportion with square root of generated noise resistance [49-52]. It concluded that induced current density at dipole D resulted in better and enhanced B_1. However, this induced current density became the cause of more power dissipation at dipole D, which yielded in generation of more noise resistance and finally decayed SNR. That's why optimized position of MR coil in accordance with distance of dipole D was recommended for better results in both received SNR and B_1. Further, we calculated power dissipation as;

$$\left|I_{ind}\right|^2 R_{noise} = R_e \int E^{ind} J^{ind} d_s = R_e \int j\omega\varepsilon_0\varepsilon_r \left|E^{ind}\right|^2 d_s \tag{23}$$

Where *Iind* was induced current at dipole D because of constant current intensity I generated by MR coil. R_{noise} was noise resistance due to intrinsically thermally generated noise currents because of power dissipation at D. E^{ind} was reflected induced electric field because of was induced current density at dipole D due to I. J^{ind} is induced current density which was proportional to I_{ind} (Figure 5).

Finally SNR was derived at dipole D for the given experimental setup depicted in Figure 5, with or without the presence of 0 μ magnetic polarizer in the setup.

$$SNR = \frac{B_z / I_{ind}}{\sqrt{R_{noise}}} \tag{24}$$

Polarizer facing X-axis and composed of 6 PCB sheets with dimensions 120 × 120 × 5 mm^3, contained 24 × 24 cubic unit cells

$(R_{P1} = R_{P2} = R_{P3})$ (Ω)	$(L_{P1} = L_{P2} = L_{P3})$ (nH)	$(C_{P1} = C_{P2} = C_{P3})$ (pF)	$M_{LP12} = M_{LP23} = M_{LP13}$(nH)
0.12	0.22	28.58	2.55
R_P' (Ω)	L_P'(nH)	C_P'(pF)	M'_{LP}(nH)
0.041	0.0734	85.70	7.64

Table 1: Calculations of C_P, L_P, R_P, M_{LP} of 0 μ SRR MM magnetic reflector unit cell.

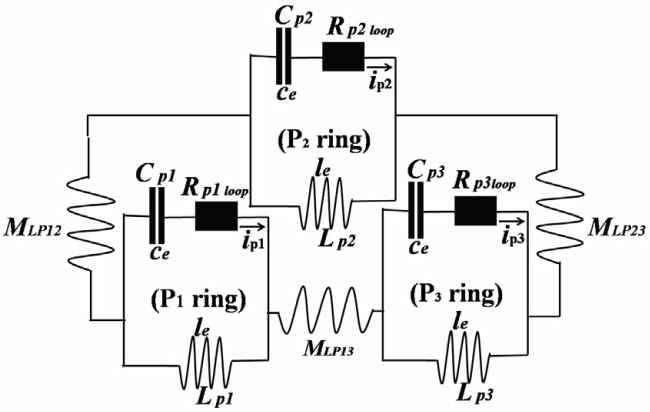

Figure 4: Equivalent Circuit model of Figure 3(a), where unit cell composed of three periodically arranged 0 μ polarizer SRR magnetically coupled rings making RLC circuit.

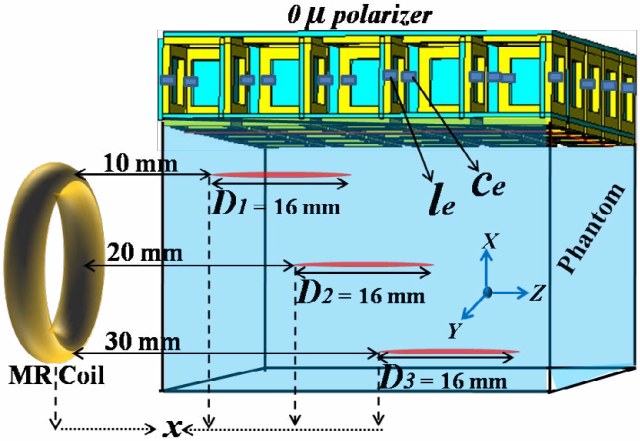

Figure 5: Experimental setup for MRI test bed , where MR coil of diameter d_M facing Z-axis and placed at distance x from magnetic dipoles D_1, D_2, D_3. 0 μ magnetic polarizer facing X-axis and placed at the top of phantom as shown. l_e, c_e were inductor element, capacitor elements of magnetic polarizer respectively.

loaded with l_e, c_e. Those cubic unit cells had repetition of 5 mm with overall 3456 SRR's. The phantom with its directions in Z-axis and with dimensions 120 × 120 × 150 mm^3, with phantom's relative permittivity ε_r =90-j197 [51]. Magnetic dipoles D_1, D_2 and D_3 were facing Z-axis with same dimensions 2 × 2 × 16 mm^3 and at optimized distances x =10 mm for D_1, x=20 mm for D_2 and x=30 mm for D_3 from MR coil, respectively with same relative permittivity as phantom. MR coil was placed at the distance x=10 mm from phantom surface which was same as the distance of D_1 from MR coil. Throughout in the simulations for polarizer, we used μ_r=0.02+j0.1, as explained in section 3. Configuration of magnetic resonance coil was already mentioned in section 2, where r_M=22 mm at t_M=2 mm with r'_M= mm was used.

Astute inspection of Figures 6a-6i showed that B-field was rejected, controlled and enhanced in the presence of 5 mm thick 0 μ polarizer. It was observed in Figure 6a for dipole D_1 that initially B-field was higher even without using polarizer. It was obvious that D_1 was much exposed {near} to the MR coil in comparison with D_2 and D_3 and that's why intensity of B-field at D_1 due to enhanced power dissipation, and induced current resulted in high values at D_1 even when polarizer was not used (Figure 6b). It meant that for the dipoles positioned like D_1, initially, polarizer was not effective to enhance B-field up to certain distance. However it was observed for D_1, that B-field started increasing at distance x=9-15 mm in the presence of polarizer (Figure 6a). This fact could be understandable in Figure 6c. We know that enhanced power dissipation yielded in heating and resulted in more thermally noise generation around the dipole which was near the MR coil due to intrinsically thermally generated noise currents, which resulted in increased noise resistance and decayed SNR. We observed that polarizer locally surpassed SNR at D_1, Figure 6c which immediately enhanced B-field at D_1 at the distance x=9-15 mm in the presence of polarizer, Figure 6a, where field intensity due to MR coil started weakening. At D_2 and D_3, we observed that B-field surpassed its values in presence of polarizer in comparison to its absence, (Figures 6d-6g) even power dissipation was higher due to field intensity of MR coil in the absence of polarizer (Figures 6e-6h). But due to weakening of field intensity of MR coil at D_2 and D_3, polarizer in its presence, locally enhanced SNR at D_2 and D_3, and reduced noise resistance which was the cause of creating intrinsically thermally generated noise currents because of high power dissipation (Figure 6f- 6i). This significance not only yielded in reduced power dissipation (Figures 6e-6h) and heating effect at D_2 and D_3, but also improved B-field at those positions and reduced SAR (Figures 6d-6g).

Safety aspects depended on the absorption of the electromagnetic (EM) energy and power dissipation which could be attributed as SAR (specific absorption ratio) at the scanned region inside the human body

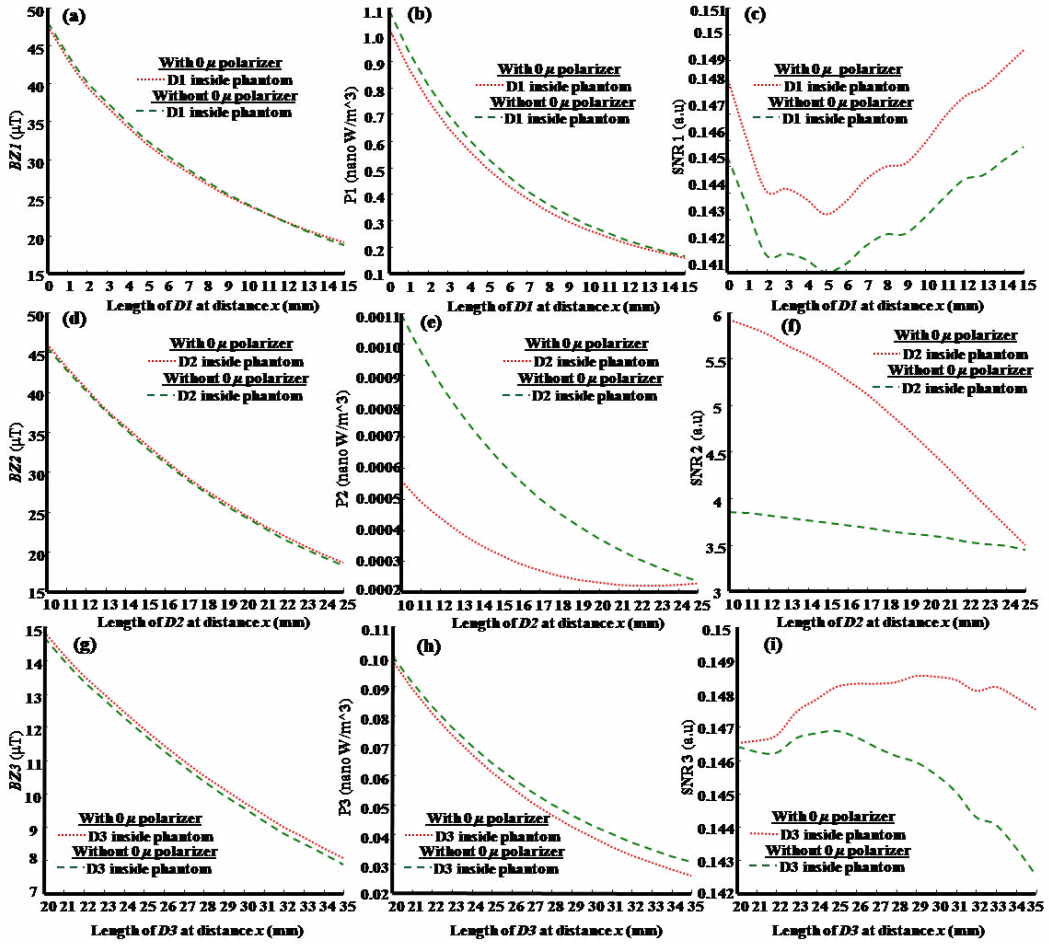

Figure 6: With or without 5 mm thick 0 μ magnetic polarizer as depicted in Fig.(5), (a, d, g) *B*-field, (b, e, h) Power dissipation, (c, f, i) SNR, at dipole D_1 with length 16 mm and thickness 2×2 mm facing towards Z-direction at the distance x=10 mm from MR coil, at dipole D_2 with length 16 mm and thickness 2×2 mm facing towards Z-direction and at x=20 mm from MR coil, at dipole D_3 with length 16 mm and thickness 2×2 mm facing towards Z-direction and at x=30 mm from MR coil respectively. (D_1 starts from phantom surface with length 0-15 mm, D_2 with length 10-25 mm and D_3 with length 20-35 mm towards Z direction respectively). MR coil facing Z- axis with diameter d_M =44 mm and thickness, t_M=2 mm was used for analysis.

during their MRI scanning [52]. The large SAR value yielded to heat the human tissue due to radio frequency (RF) pulses generated by MR coil and could be harmful for the biological structure of tissue. SAR was proportional to the square of electric field applied to MR coil [53] (Figure 6).

We observed that applied electric E field was concentrated at the edges of the MR coil loop antenna and it had the lowest values at middle of MR coil, which meant that electric field did not encountered the magnetic field in the middle of the loop as the transversal Eigen modes for electric field were disappeared in that area and in result SAR was reduced in that region, say; middle area of the loop [30-54]. This aspect provided the possibility to redistribute RF field and reduce SAR in the region of interest which in resulted not only locally enhanced the magnetic field in that region but also improved SNR. Furthermore the technique removed electric field, substantially decreased the power dissipation and EM energy absorption at ROI which could the best optimized technique to avoid the damages caused from human tissue heating inside human body. This effect could be clearly seen at dipole D_2 positioned in the middle of the MR coil shown in Figure 5, and analyzed in Figures 6e-6f. We observed substantial decrease in power dissipation and locally increase in SNR at D_2, which was positioned at x=20 mm from MR coil loop antenna. We also observed that polarizer enhanced the magnetic field at D_2 while substantially keeping power dissipation low and high SNR in comparison to the results in its absence. We concluded that the efficiency of polarizer could be increased by choosing the optimized position of MR coil, in the way to exactly position ROI at the center of the coil. That yielded in reducing SAR, power dissipation, increasing *B*-field and SNR at ROI (Figure 7).

Figure 7 depicted noise resistance analysis at magnetic dipoles D_1, D_2 and D_3 in the presence of polarizer. As we have mentioned above, that noise resistance deeply impacted SNR and this effect could also be deduced from eqn. (24). We observed more noise generation at dipoles positioned near to MR coil. So dipoles experienced more noise resistance in comparison to the dipoles positioned at farther distances from MR coil in the setup of Figure 5. It was due to intrinsically thermally generated noise currents which limited SNR at ROI which were near to MR coil. This effect could be clearly seen in Figure 6, that larger power dissipation quickly decreased SNR at the dipoles. At the optimized position of MR coil with respect to D_2, in the presence of polarizer, we observed an ample decrease of noise resistance, power dissipation, and enhanced SNR (Figure 7, Figures 6e and 6f).

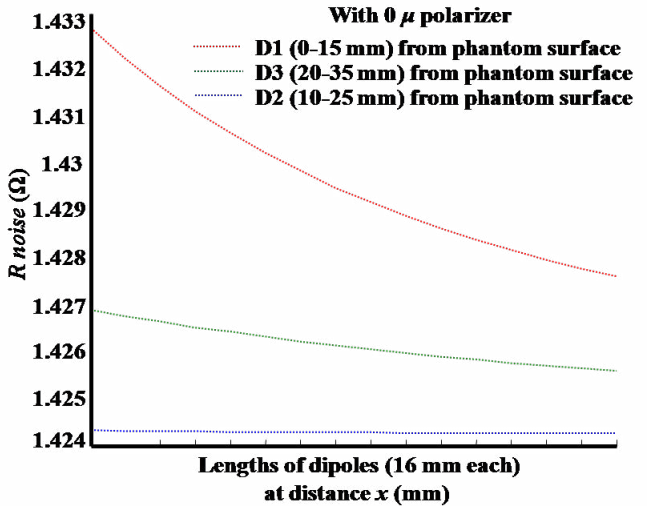

Figure 7: Noise resistance analysis at magnetic dipoles D_1, D_2 and D_3 in the presence of 0 μ magnetic polarizer.

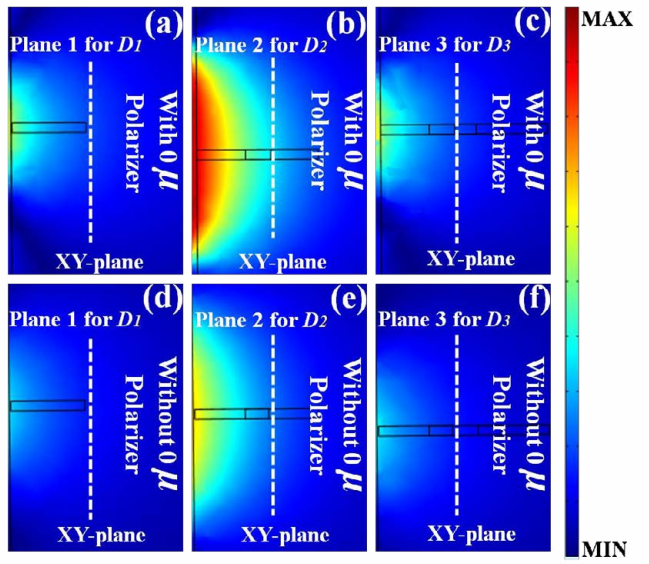

Figure 8: SNR profiles along the XY-plane for magnetic dipoles D_1, D_2, D_3 in the presence (a, b, c) and in absence (d, e, f) of 0 μ magnetic polarizer metamaterial.

Figure 8 depicted SNR profiles in XY-plane along white dashed line with intensity of SNR at three dipole positions D_1, D_2 and D_3, respectively. Figures 8a-8c confirmed stronger SNR profiles at all considered dipole positions in the presence of our designed 0 μ magnetic polarizer as compared to its absence, as the polarizer rejected and controlled the signal into the phantom and increased signal's intensity coming from polarizer's direction (Figure 8).

Conclusion

We designed a novel and compact 0 μ magnetic polarizer SRR metamaterial fully operational at 63.85 MHz. The design more specifically reduced specific absorption ratio (SAR) effects as well as improved image quality for 1.5 T MRI systems. Polarizer was the combination of SRR copper loops and loaded with lumped capacitor c_e and inductor l_e with compact thickness of only 5 mm. It could efficiently distort, reject, control and redistributed the RF field inside phantom {real case was human body} and could locally enhanced magnetic field by increasing SNR and reducing noise resistance at ROI without increasing the static magnetic field of external MR coil of MRI system. This unique combination of lumped elements with copper loops has not been used before for such applications. Polarizer exploited nonlinear characteristics of the lumped elements especially inductor element which exhibited minimized propagation losses, strong mutual inductance and uniformity of currents between SRR rings. In result, amplitude of the incoming decaying signal was reconstructed due to polarizer's material's property at frequency of resonance. Furthermore, polarizer allowed an opportunity for the construction of tunable magneto-inductive SRR metamaterial at very low working frequencies. In addition we highlighted the significance of polarizer in the optimized MRI test bed setup as it improved magnetic field and removed induced electric field at different dipole positions inside phantom (real case human body) in the setup which reduced the power dissipation at that dipole positions finally resulted in improved SNR and reduced SAR at dipoles. The design improved the safety aspects to avoid human tissue heating due to large power dissipation because of radio frequency RF pulses generated by MR coil which could be harmful for the biological structure of tissue.

Future prospect of our designed magnetic polarizer SRR metamaterial can be the fabrication of smart clothes for patients using MRI scanning, which will enhance image resolution inside human body.

Acknowledgement

The authors are grateful to the partial supports from NSFCs 61271085. (National Natural Science Foundation of China)

Declarations

All the work has been performed at center of optical and electromagnetic research, department of optical engineering, Zhejiang University, Hangzhou, China. The authors are grateful to the partial supports from NSFCs 61271085 (National Natural Science Foundation of China).

Competing Interest

The authors declare that they have no financial competing interests with this manuscript. This work is accomplished at center of optical and electromagnetic research {COR&R}, Zhejiang University, China and partial supports from NSFCs 61271085 (National Natural Science Foundation of China). There is no any kind of financial gain or loss is involved with this work. We are not applying for any patent related to the content.

The authors declare that they have no non-financial competing interests with this manuscript.

Author Contributions

Dr. Hassan Ali generated an idea to design 0 permeability metamaterials which are more compact, robust and efficient in a sense to enhance magnetic field at designated part of the body, without increasing specific absorption ratio. Under this regard, whole idea was discussed with Professor Dr. Hu Jun and Professor Dr. Erik Forsberg, who not only appreciated the idea but also helped to refine design's parameters during all progress of this work. They also provide all useful resources and environment (technical and financial) which was necessary to accomplish this work.

Funding

Center of optical and electromagnetic research {COR&R}, Zhejiang University, China partial supports from NSFCs 61271085 (National Natural Science Foundation of China).

References

1. Lauterbur PC (1973) Image Formation by Induced Local Interactions: Examples Employing Nuclear Magnetic Resonance. Nature 242: 190-191.

2. Hendee WR (1999) Physics and applications of medical imaging. Rev Mod Phys.
3. Logothetis NK (2008) What we can do and what we cannot do with fMRI. Nature (London) 453: 869-878.
4. Ma D, Gulani V, Seiberlich N, Liu K, Sunshine J, et al. (2013) Magnetic resonance fingerprinting. Nature 495: 187-192.
5. Degen CL, Poggio M, Mamin HJ, Rettner CT, Rugar D (2009) Nanoscale magnetic resonance imaging. PNAS 106: 1313-1317.
6. Brown RW, Cheng YCN, Haacke EM, Thompson MR, Venkatesan R (1999) Magnetic Resonance Imaging: Principles and Sequence Design. Wiley.
7. Vaughan T, DelaBarre L, Snyder C, Tian J, Akgun C, et al. (2006) 9.4T human MRI: preliminary results. Magn Reson Med 56: 1274-1282.
8. Jouvaud C, Abdeddaim R, Larrat B, de Rosny J, (2016) Volume coil based on hybridized resonators for magnetic resonance imaging. Appl Phys Lett 108: 023503.
9. Sodickson DK, Manning WJ (1997) Simultaneous acquisition of spatial harmonics (SMASH): fast imaging with radiofrequency coil arrays. Magn Reson Med 38: 591-603.
10. Pruessmann KP, Weiger M, Scheidegger MB, Boesiger P (1999) SENSE: Sensitivity Encoding for Fast MRI. Magn Reson Med 42: 952-962.
11. Roemer PB, Edelstein WA, Hayes CE, Souza SP, Mueller OM (1990) The NMR phased array, Magn Reson Med 16: 192-225.
12. Brunner DO, De Zanchei N, Frohlich J, Paska J, Pruessmann K (2009) Travelling-wave nuclear magnetic resonance. Nature 457: 994-998.
13. Andreychenko A, Kroeze H, Klomp DW, Lagendijk JJ, Luijten PR, et al. (2013) Coaxial waveguide for travelling wave MRI at ultrahigh fields. Magn Reson Med 70: 875-884.
14. Kuperman V (2000) Magnetic Resonance Imaging: Physical Principles and Applications. Academic Press, San Diego.
15. Hogemann D, Josephson L, Weissleder R, Basilion JP (2000) Improvement of MRI Probes To Allow Efficient Detection of Gene Expression. Bioconjugate Chemistry 11: 941-946.
16. Stafford RJ (2005) TU-B-I-617-01: High Field MRI-Technology, Applications, Safety, and Limitations. Med Phys 32: 2077-2077.
17. Solis SE, Wang R, Tomasi D, Rodriguez AO (2011) A multi-slot surface coil for MRI of dual-rat imaging at 4 T. Phys Med Biol 56: 3551- 3561.
18. Hayes CE, Edelstein WA, Schenck JF, Mueller OM, Eash M (1985) An efficient, highly homogeneous radio frequency coil for whole body NMR imaging at 1.5T. J Magn Reson Med 63: 622-628.
19. Katscher U, Bornert P (2006) Parallel RF transmission in MRI. NMR Biomed 19: 393-400.
20. Belov P, Zhao Y, Sudhakaran S, Alomainy A, Hao Y (2006) Experimental study of the subwavelength imaging by a wire medium slab. Appl Phys Lett 89: 262109.
21. Pendry JB (2000) Negative Refraction Makes a Perfect Lens. Phys Rev Lett 85: 3966-3969.
22. Smith DR, Pendry JB, Wiltshire MCK (2004) Metamaterials and negative refractive index. Science 305: 794-799.
23. Baena JD, Jelinek L, Marques R, Silveirinha M (2008) Unified homogenization theory for magnetoinductive and electromagnetic waves in split-ring metamaterials. Phys Rev A 78: 013842.
24. Ali H, Jun H, Abbas A, Tariq M (2017) μ Compact magnetic metamaterial lens for 0.35-T MRI. Journal of Optics 46: 436-445.
25. Cai W, Shalaev V (2010) Optical Metamaterials: Fundamentals and Applications. Springer, New York.
26. Freire M, Marques R, Jelinek L (2008) Experimental demonstration of a μ =−1 metamaterial lens for magnetic resonance imaging. Appl Phys Lett 93: 231108.
27. Marques R, Mesa F, Martel J, Medina F (2003) Comparative analysis of edge- and broadside- coupled split ring resonators for metamaterial design-theory and experiments. IEEE Trans Antennas Propag 51: 2572-2581.
28. Ali H, Forsberg E, Jun H (2016) Sub-Wavelength Imaging with BC-SRRs Metamaterial Lens for 1.5-T MRI. Appl Magn Reson 47: 539-554.
29. Syms PRA, Floume T, Young I, Solymar L, Rea M (2010) Flexible magnetoinductive ring MRI detector: Design for invariant nearest-neighbour coupling. Metamaterials 4: 1-14.
30. Radu X, Garray D, Craeye C (2009) Toward a wire medium endoscope for MRI imaging. Metamaterials 3: 90-99.
31. Ali H, Forsberg E, Jun H (2016) Brain imaging with slotted hybridized magnetic metamaterial hat at 7-T MRI. Appl Magn Reson 48: 67-83.
32. Babic S, Akyel C (2008) Magnetic Force Calculation between Thin Coaxial Circular Coils in Air. Mag IEEE Trans 44: 445-452.
33. Garcia N, Munoz M, Ponizovskaya EV, Nieto-Vesperinas M (2002) Zero Permeability Materials (ZmuM): A way out of the “Left Handed Materials” trap. Cornell University Library.
34. Jelinek L, Marqués R, Freire M (2009) Accurate modeling of split ring metamaterial lenses for magnetic resonance imaging applications J Appl Phys.
35. Chen XD, Grzegorczyk TM, Wu BI, Pacheco J, Kong JR (2004) Robust method to retrieve the constitutive effective parameters of metamaterials. Phys Rev E Stat Nonlin Soft Matter Phys.
36. Syms RRA, Solymar L, Young IR (2008) Three-frequency parametric amplification in magneto-inductive ring resonators. Metamaterials 2: 122-134.
37. Sydoruk O, Shamonina E, Solymar L (2007) Parametric amplification in coupled magnetoinductive waveguides. J Phys D Appl Phys 40: 6879.
38. Hadjicosti K, Sydoruk O, Maier SA, Shamonina E, (2015) Surface polaritons in magnetic metamaterials from perspective of effective-medium and circuit models. J Phys 117: 163910.
39. Valkenburg V (1958) Network Analysis. Prentice-Hall, London.
40. Lapine M, Jelinek L, Marques R, Freire M (2010) Exact modelling method for discrete finite metamaterial lens. IET Microw Antennas Propag 4: 1132-1139.
41. Hall SH, Heck HL (2009) Advanced signal integrity for high- speed digital designs. Hoboken Wiley, New Jersey.
42. Balanis CA (2012) Advanced Engineering Electromagnetics. Wiley, Hoboken, New Jersey.
43. Reed DG (2005) ARRL handbook for radio communications. Newington, CT: American Radio Relay League.
44. Thierauf SC (2004) High-speed circuit board signal integrity. Norwood, MA: Artech House.
45. Wensong W, Chen Y, Yang S, Zheng X, Cao Q (2015) Design of a broadband electromagnetic wave absorber using a metamaterial technology. J Electromagn Waves and Appl 29: 2080-2091.
46. Tan S, Yan F, Sing L, Cao W, Xu N, et al. (2015) Terahertz metasurfaces with a high refractive index enhanced by the strong nearest neighbor coupling. Optics Express 23: 29222-29230.
47. Algarin JM, Lopez MA, Freire MJ, Marques R (2011) Signal-to-noise ratio evaluation in resonant ring metamaterial lenses for MRI applications. New J Phys.
48. Hoult DI, Richards RE (1976) The signal-to-noise ratio of the nuclear magnetic resonance experiment. J Magn Reson 24: 71-85.
49. Edelstein WA, Glover GH, Hardy CJ, Redington RW (1986) The intrinsic signal-to-noise ratio in NMR imaging. Reson Med 3: 604-618.
50. Rosa FB, Grover FW (1948) Bulletin of the Bureau of Standards. Government Printing Office, Washington.
51. Landau LD, Lifschitz EM (1984) Electrodynamics of Continuous Media. Pergamon Press, Oxford.
52. Freire M, Jelinek L, Marques R, Lapine M (2010) On the applications of μr = −1 metamaterial lenses for magnetic resonance imaging. J Magn Reson 203: 81-90.
53. Slobozhanyuk AP, Poddubny AN, Raaijmakers AJE, Van den Berg CAT, Kozachenko AV, et al. (2015) Enhancement of magnetic resonance imaging with metasurfaces. Cornell University Library.
54. Slobozhanyuk AP, Poddubny AN, Krasnok AE, Belov PA (2014) Magnetic Purcell factor in wire metamaterials. Appl Phys Lett 104: 161105.